



Showcasing research from Professor Derek Patton's laboratory, School of Polymer Science and Engineering, University of Southern Mississippi, Hattiesburg, MS, USA.

Cyclic ketal bridged bisepoxides: enabling the design of degradable epoxy-amine thermosets for carbon fiber composite applications

Degradable epoxy-amine thermosets derived from a series of cyclic-ketal based bisepoxide monomers offer mechanical properties comparable to non-degradable commercial variants yet fully degrade under low pH aqueous conditions, facilitating the recovery of pristine carbon fibers from fiber reinforced polymer composites and the potential recovery and reuse of ketone building blocks. This work illustrates the possibility of achieving balance between real-world application and effective end-of-use material recovery strategies.

As featured in:



See Derek L. Patton *et al.*,  
*RSC Appl. Polym.*, 2023, 1, 254.



Cite this: *RSC Appl. Polym.*, 2023, **1**, 254

## Cyclic ketal bridged bisepoxides: enabling the design of degradable epoxy-amine thermosets for carbon fiber composite applications†

Benjamin M. Alameda,<sup>1</sup> Margaret S. Kumler,<sup>2</sup> J. Scott Murphy,<sup>3</sup> Jeffrey S. Aguinaga<sup>4</sup> and Derek L. Patton<sup>1</sup>\*

A series of degradable epoxy-amine thermosets was developed using novel cyclic-ketal based bisepoxide monomers and a commercially available diamine. By tailoring the design of the ketal bridge, we fabricated thermosets that undergo complete degradation with tunable degradation profiles in low pH conditions while maintaining stability in mildly acidic to basic pH conditions. The thermomechanical and mechanical properties of these degradable thermosets were comparable to a non-degradable commercial variant, offering similar or superior performance. We further demonstrated the application of these degradable thermosets in the construction of carbon-fiber reinforced polymer (CFRP) composites. Using aqueous conditions, the polymer matrix could be fully degraded in low pH conditions, enabling the recovery of pristine carbon fibers. This work showcases the potential of cyclic-ketal based thermosets in achieving a delicate balance between robust performance in practical composite applications and efficient end-of-use recovery strategies. The successful recovery and reuse of high-quality carbon fibers from CFRPs not only contribute to resource sustainability but also offer economic advantages by potentially reducing material costs and waste.

Received 23rd June 2023,  
Accepted 10th August 2023

DOI: 10.1039/d3lp00095h

rsc.li/rscapppolym

### Introduction

Epoxy-amine thermosets are ubiquitous in the production of coatings,<sup>1</sup> electronic packaging,<sup>2</sup> and carbon-fiber reinforced polymer composites (CFRPs) for the automotive, aerospace, and energy sectors due to their exceptional mechanical strength, temperature and chemical stability, and ease of polymerization.<sup>3</sup> However, the covalently crosslinked networks that confer these advantageous properties also render them non-reprocessable and pose serious challenges for chemical recyclability at the end-of-use, thereby exacerbating the escalating issue of plastic pollution.<sup>4</sup> For CFRPs, these end-of-use limitations not only irreversibly commit non-renewable resources to either pyrolysis processes or landfills, but also lead to the permanent disposal of costly carbon fibers that could otherwise be repurposed in the fabrication of new composite materials.<sup>4–6</sup> While reclaiming carbon fibers from thermosets has been explored,<sup>7,8</sup> recovering high quality fibers remains difficult and energy intensive.<sup>5,9</sup> Many of the recovery methods such as pyrolysis, solvolysis, and mechanical pro-

cesses are harsh and can damage the carbon fibers – rendering the fibers sub-par for reuse in new composite components.<sup>10–12</sup>

A promising strategy for the successful recovery of carbon fibers hinges on the design and use of degradable thermosets – materials with labile bonds that breakdown in response to specific stimuli (*e.g.*, pH,<sup>7</sup> light<sup>13</sup>) enabling the subsequent retrieval of the carbon fibers. Covalent adaptable and/or vitrimer thermosets are also of interest but may be considered a subset of degradable materials in the context of carbon fiber recovery.<sup>14,15</sup> A variety of chemistries, including acetals,<sup>10,11,16–18</sup> ketals,<sup>19</sup> esters,<sup>20</sup> and imines,<sup>21–23</sup> have been employed in the design of hydrolytically susceptible epoxy-amine thermosets for CFRPs. Among these chemistries, ketals offer a compelling choice for the development of labile linkages in epoxy-amine thermosets, given their straightforward synthesis, the diversity of ketone precursors available for ketal formation, and their propensity to degrade into neutral by-products (*e.g.*, ketones and alcohols) under acidic conditions. The hydrolysis of ketals proceeds *via* a well-documented mechanism, with the formation of a resonance-stabilized carbenium ion intermediate as the rate-determining step. As a result, the hydrolytic stability of ketals can be finely tuned based on steric, electronic, and structural (*e.g.*, cyclic, acyclic) factors.<sup>24–27</sup> Our previous work with poly( $\beta$ -thioether ester

School of Polymer Science and Engineering, University of Southern Mississippi, Hattiesburg, MS 39406, USA. E-mail: derek.patton@usm.edu

† Electronic supplementary information (ESI) available: NMR analysis of monomers and monomer intermediates. See DOI: <https://doi.org/10.1039/d3lp00095h>





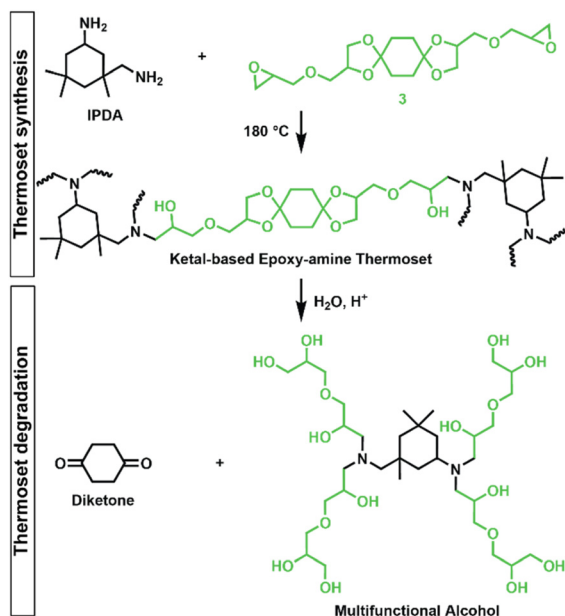


**Fig. 2** Synthesis of epoxy-amine ketal thermosets from monomer **3**/IPDA and degradation into diketone and multifunctional alcohol by-products (drawn as idealized structure that would be derived from quantitative hydrolysis of a fully converted epoxy-amine network).

an oven: initially at 75 °C for 2 h, followed by 120 °C for 2 h, and finally at 180 °C for 2 h.

Differential scanning calorimetry (DSC) and dynamic mechanical analysis (DMA) were employed to investigate the glass transition temperatures ( $T_g$ ) of the networks to determine the ultimate use temperatures of the degradable ketal-based networks compared to the commercially available **HP** thermoset. As depicted in Fig. 3a, DSC analysis revealed a single second-order endotherm in the thermogram for each polymer network, indicative of the  $T_g$ . The determined  $T_g$ s were 94.1 °C for **3P**, 96.3 °C for **6P**, and 80.7 °C for **9P**. The  $\tan \delta$  ( $E''/E'$ ) and storage moduli ( $E'$ ) curves obtained by DMA for thermosets **3P–9P** are provided in Fig. 3b. The mechanical  $T_g$ , taken as the peak of the  $\tan \delta$  curve, was observed at 111 °C for **3P**, 105 °C for **6P**, and 86.3 °C for **9P**, and the **HP** network at 107 °C. **9P** exhibited a consistently lower  $T_g$  than the other thermoset compositions, which may be attributed to the additional degree of rotation from the *para*-positioned  $\sigma$ -bonds of monomer **9**. Likewise, monomers **3** and **6** have tricyclic and bicyclic structures, respectively, that tend to increase network rigidity and  $T_g$ . The network structure was determined to be homogenous with all ketal-based networks displaying narrow  $\tan \delta$  peaks; the only exception being **HP**, which exhibited a bimodal peak that is presumably due to mixed aromatic and aliphatic network composition due to incomplete hydrogenation of the monomer (Fig. 3a and Table 1). While the structure of the ketal monomer influenced  $T_g$ , it had relatively little effect on the glassy and rubbery moduli, as indicated in Fig. 3b. Fig. 3c presents the stress–strain curves for the epoxy-amine thermosets, with the corresponding mechanical data



**Fig. 3** Characterization of **3P**, **6P**, **9P**, and **HP** via (a) DSC, (b) DMA, (c) mechanical testing, and (d) TGA.

quantified in Table 1. The **3P** and **9P** thermosets demonstrated the highest Young's modulus values, at  $632 \pm 36$  and  $676 \pm 12$  MPa, respectively. In contrast, the **6P** network exhibited the lowest Young's modulus, at  $462 \pm 10$  MPa. These trends in tensile properties align well with the glassy storage moduli trends observed *via* DMA and the properties were comparable to those of the **HP** network. All samples exhibited some degree of yield after peak stress typical of some epoxy-amine thermosets.<sup>28</sup> Notably, the **6P** network, characterized by its bicyclohexyl structure, displayed the greatest strain at break and toughness. This can be attributed to a distortional energy-absorbing mechanism, which arises from conformational changes such as chair/boat ring flips in the cyclohexyl linkages.<sup>29</sup> Similar trends were previously observed with this bicyclohexyl structure in thiol-ene photopolymer networks.<sup>25</sup>



**Table 1** Summary of mechanical, thermomechanical and thermal degradation data for ketal-based thermosets

	3P	6P	9P	HP
Young's modulus (MPa)	632 ± 35.6	462 ± 9.94	676 ± 12.3	583 ± 32.4
Strain at break (mm mm <sup>-1</sup> )	0.181 ± 0.014	0.267 ± 0.038	0.225 ± 0.049	0.208 ± 0.015
Peak stress (MPa)	71.2 ± 2.77	60.3 ± 2.69	65.1 ± 1.10	66.1 ± 3.17
T <sub>g</sub> DSC (°C)	94.1	96.3	80.7	96.8
T <sub>g</sub> DMA (°C)	111	105	78	107
Glassy modulus (MPa, 25 °C)	2264	1552	2651	2645
Rubbery modulus (MPa, 150 °C)	8.62	9.23	11.4	9.46
FWHM (tan δ)	15.6 ± 0.213	14.1 ± 0.170	11.9 ± 0.155	N/A (bimodal)
T <sub>d, 10%</sub> (°C)	311	327	326	306

Thermogravimetric analysis was utilized to assess the thermal stability of the ketal-based epoxy-amine thermosets under air atmosphere. The thermal degradation profiles for each thermoset, depicted in Fig. 3d, exhibited similar behavior, demonstrating a relatively high resistance to thermal degradation. The temperature at which a 10% mass loss ( $T_{d,10}$ ) occurred ranged from 311 °C to 327 °C (Table 1). All samples displayed a single mass loss transition, with degradation leaving less than 15% char beyond 500 °C.

### CFRP construction and mechanical testing

CFRP laminates (3 layers of 3k 2 × 2 carbon fiber twill weave oriented in alternating 0° and 90° orientations) were prepared *via* a conventional hand-laminating/vacuum bagging technique using the three degradable ketal-based epoxy monomers 3–9 with IPDA, along with HP to compare the overall mechanical properties. An exemplar CFRP panel is shown in Fig. 4a. Each panel was then cut into 25 mm × 254 mm strips for mechanical testing in accordance with ASTM D3039 (Fig. 4b). The resin-to-fiber weight ratio was maintained to enable a direct comparison of mechanical performance. Prior to mechanical testing, TGA was employed to analyze samples from each panel to calculate the final resin loading after cure and post-processing. Given that carbon fibers are thermally stable up to approximately 800 °C,<sup>30</sup> TGA experiments were conducted up to 700 °C to pyrolyze the matrix and ascertain the matrix-to-fiber weight ratio of each CFRP. The onset of matrix degradation occurred around 300 °C, mirroring the behavior of the resin without carbon fiber (Fig. 3d). The resin-to-fiber ratio for all panels was found to be similar and within the typical range for CFRPs,<sup>31,32</sup> with resin loading amounts of 33.4% for 3P CFRP, 36.0% for 6P CFRP, 36.9% for 9P CFRP, and 34.6% for HP CFRP (Fig. 4c). Given the minimal differences among the panels, a direct comparison of mechanical properties was feasible.

Fig. 4d shows the stress *vs.* strain curves for each CFRP composition in triplicate, with average values provided in Table 2. 3P CFRP and 9P CFRP exhibited the highest Young's modulus at 44.6 ± 1.9 GPa and 46.6 ± 4.6 GPa – generally reflecting the trends observed in mechanical properties for the resin only samples. However, similar Young's modulus values were observed for all composite compositions, which can be



**Fig. 4** (a and b) Photos of CFRP composite panel (254 mm × 254 mm) prepared and cut (25 mm × 254 mm) for mechanical testing. (c) Thermogravimetric analysis to determine resin-to-fiber ratio after composite cure and processing. (d) Stress–strain curves for CFRP composites.

attributed to a mechanical response dominated by the longitudinal tensile properties of the vertically aligned fibers within the samples. The degradable ketal-based CFRPs generally surpassed the HP control in terms of average strain at break and ultimate tensile strength. Notably, 9P CFRP demonstrated the highest strain at break ( $0.0169 \pm 0.000488$  mm mm<sup>-1</sup>) and the highest tensile strength ( $584.7 \pm 12.9$  MPa). Although numerous factors influence the mechanical performance of CFRPs,<sup>33</sup> the superior performance of 9P CFRP may be attributed to enhanced matrix–fiber interactions facilitated by the aromatic content of the 9P resin.



**Table 2** Mechanical properties of the 3P–HP CFRP composites

Sample	Young's modulus (GPa)	Strain at break (mm mm <sup>-1</sup> )	Tensile strength (MPa)
3P CFRP	44.6 ± 1.9	0.0156 ± 0.0017	550.7 ± 25.1
6P CFRP	39.9 ± 1.8	0.0137 ± 0.0006	493.9 ± 20.3
9P CFRP	46.6 ± 4.6	0.0169 ± 0.0005	584.7 ± 12.9
HP CFRP	41.8 ± 3.9	0.0128 ± 0.0005	465.9 ± 15.5

### Thermoset degradation

The degradation of the ketal-based thermosets is depicted in Fig. 2 (with further elaboration in Fig. 7). To discern the impact of ketal structure on hydrolytic stability of the monomers independent of influences such as polymer network architecture and hydrophobicity,<sup>34–36</sup> evaluation of degradation kinetics were initially conducted on intermediate products 2, 5, and 8 using <sup>1</sup>H-NMR. Here, we used the alcohol intermediates as surrogates for the monomers to circumvent complications in the observed kinetics that could arise from the acid-catalysed ring-opening of the monomer epoxide groups.<sup>37</sup> Fig. 5a presents the time-dependent <sup>1</sup>H-NMR spectra for the hydrolysis of intermediate 2. The extent of hydrolysis over time was quantified by comparing the ratio of the ketal (indicated by peak label A) and ketone (indicated by peak label B) peaks. The kinetic curves obtained from these time-resolved NMR spectra are shown in Fig. 5b. Below 50% hydrolysis, we observed the expected trend in ketal stability with 2 exhibiting the greatest stability (and thus slowest rate of hydrolysis), followed by 5 and 8 – results that are in good agreement with our previous work with poly(β-thioether ester ketals).<sup>25</sup> However, beyond 50% hydrolysis, the kinetic curves for 5 and 8 intersect, suggesting a change in hydrolytic stability of these ketal structures. This abrupt change in kinetics is more apparent by plotting the natural log of the ketal concentration vs. time (Fig. 5c). Unlike ketals 2 and 5, which both exhibit pseudo-first order degradation kinetics characterized by a single linear kinetic regime ( $k_2 = 0.357 \pm 0.001 \text{ h}^{-1} \times 10^{-2}$ ,  $k_5 = 4.24 \pm 0.137 \text{ h}^{-1} \times 10^{-2}$ ), ketal 8 exhibits two distinct linear regimes – one before and another after 50% hydrolysis, denoted as (i) and (ii), respectively, as illustrated in Fig. 5c. The distinct kinetic regimes for 8 can be explained by resonance effects of the aromatic group before and after the hydrolysis of at least one ketal substituent on the aromatic ring. Substituent effects on the rates of hydrolysis of acetals and ketals have been well established,<sup>38–41</sup> where steric<sup>26,42</sup> and electronic effects<sup>27,43,44</sup> have a major influence over ketal/acetal stability. For instance, electron donating groups help stabilize the transition state of the well-established acid-catalyzed hydrolysis mechanism – resulting in more rapid hydrolysis while electron withdrawing groups destabilize the transition state, slowing hydrolysis.<sup>27</sup> In the case of ketal 8, the presence of a ketal substituent in the *para* position helps to stabilize the transition state – affording relatively quick hydrolysis of the first *para*-substituted ketal ( $k_{8(i)} = 8.03 \pm 0.08 \text{ h}^{-1} \times 10^{-2}$ ). The resultant asymmetric *para*-substituted ketone then destabilizes the carbocation transition

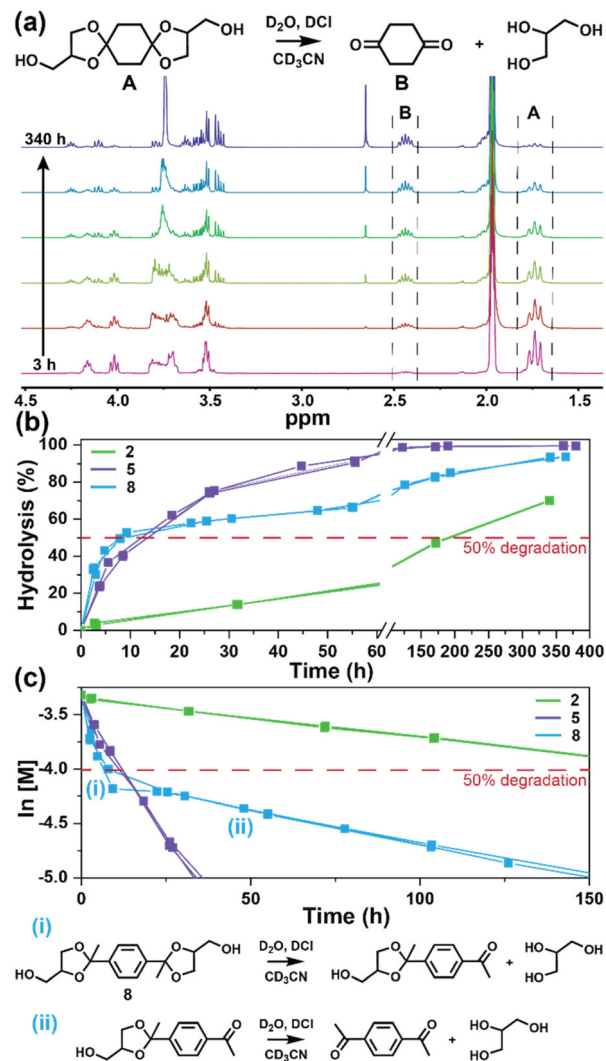


**Fig. 5** (a) Time-resolved <sup>1</sup>H-NMR spectra for the hydrolysis of intermediate 2 by monitoring the integration of (A) ketal and (B) ketone peaks over 340 h at ambient temperature (20 °C). (b) Hydrolysis kinetics plotted for 2, 5, and 8 vs. time. (c) Semilogarithmic kinetic plot for the hydrolysis of 2, 5, and 8. Two kinetic regimes and the associated structures for hydrolysis of 8 are indicated by (i) and (ii).

state through resonance – decreasing the hydrolysis rate of the second ketal by an order of magnitude ( $k_{8(ii)} = 0.600 \pm 0.036 \text{ h}^{-1} \times 10^{-2}$ ).

The influence of ketal structure on the hydrolytic stability of thermosets, as suggested by the previous hydrolysis kinetics of the small molecule intermediates, was further investigated through mass-loss experiments conducted in various aqueous environments. These included 1 M HCl (pH 0.88), acetate buffer (pH 4.07), phosphate buffered solution (PBS) (pH 7.40), and glycine/NaOH buffer (pH 11.65). The results of these mass-loss experiments are shown in Fig. 6a–d. Across the mildly acidic to basic pH solutions (4.07–11.65), negligible losses in mass were observed over 800 hours, indicating 3P, 6P, and 9P thermosets are relatively stable under such conditions. Only when submerged in highly acidic 1 M HCl did the





**Fig. 6** Mass-loss degradation versus time for 3P, 6P, and 9P in (a) glycine buffer (pH 11.65), (b) PBS buffer (pH 7.40), (c) acetate buffer (pH 4.07), and (d) 1 M HCl (pH 0.88). Experiments were conducted at ambient lab temperature (20 °C). (e) Snapshot photos of 9P disks pulled from 1 M HCl at various time intervals to illustrate surface erosion.

samples exhibit rapid mass loss (Fig. 6d). The trend in thermoset hydrolytic stability mirrored that of our small molecule degradation experiments, with 3P exhibiting the slowest degradation and 9P and demonstrating the fastest degradation. Static water contact angle measurements of the thermosets were similar (Fig. S7,† 90.3° for 3P, 88.5° for 5P, and 93.8° for 9P), suggesting that hydrophobicity of resins play a minimal role in the observed degradation profiles. All samples displayed surface-controlled erosion behavior, evidenced by consistent mass-loss profiles and retention of shape with a reduction in sample dimensions throughout the degradation process (Fig. 6e). This surface erosion behavior is a result of ketal bond cleavage occurring at a faster rate than the diffusion of solution into the bulk of the sample.<sup>34</sup> Importantly, the degradation by-products for each sample were sufficiently miscible in the aqueous degradation media to pre-

clude the use of organic cosolvents (*e.g.* THF, DMF, *etc.*), which are often necessary to facilitate efficient degradation of polymer thermosets. We gained additional insights into the composition of the degradation byproducts for 3P by performing an organic extraction ( $\text{CH}_2\text{Cl}_2$ ) of the aqueous degradation media (Fig. 7a). After separation of the layers, the aqueous fraction was neutralized with  $\text{NaHCO}_3$  prior to lyophilization. As indicated by  $^1\text{H}$  (Fig. 7b) and  $^{13}\text{C}$  NMR (Fig. 7c), the organic fraction was identified as the monomer building block 1,4-cyclohexanedione. For simplicity, the multifunctional alcohol byproduct shown in Fig. 2 is drawn to represent an ideal structure derived from quantitative hydrolysis of a fully converted epoxy-amine network. However, the aqueous fraction likely contains a mixture of multifunctional alcohol structures better represented by the distribution of products (i–iii) shown in Fig. 7a (*e.g.*, structure (ii) could arise from incomplete conversion of IDPA). FTIR of the lyophilized fraction, as shown in Fig. 7d, clearly indicates an aliphatic byproduct (2929, 2884  $\text{cm}^{-1}$ ) that carries significant hydroxyl functionality, with a broad band at 3288  $\text{cm}^{-1}$  and bands at 1037 and 1109  $\text{cm}^{-1}$  consistent with primary and secondary alcohols of an alkyoxy-1,2-propanediol structure.<sup>45</sup> The peak at 1702  $\text{cm}^{-1}$  may be attributed to either residual 1,4-cyclohexanedione or to incomplete hydrolysis of the ketal yielding a functionality represented by structure (iii) in Fig. 7.  $^1\text{H}$  NMR of the lyophilized fraction points to similar structural features derived from an IPDA framework;<sup>46</sup> however, due to the inability of effectively separate the products, only general NMR peak assignments were made. In previous work,<sup>25</sup> we demonstrated the ability to recover the ketone building blocks for use in the synthesis of new monomer, thus we did not repeat those experiments for the current work. While speculative at best, the multifunctional alcohol byproducts may find use as polyol synthetic additives or as precursors for biolubricants.<sup>47</sup>

### CFRP stability, degradation, and fiber recovery

While numerous strategies for thermoset degradation and carbon fiber recovery have been reported in the literature, most of these methods rely on a combination of organic solvents (*e.g.*, DMF,<sup>48</sup> THF,<sup>49</sup> methanol,<sup>14</sup> acetone,<sup>7,17</sup> *etc.*) and aqueous acid or base to effectively degrade the polymer matrix. These approaches, while effective, often introduce additional complexities and environmental concerns. Here, we demonstrate an approach that leverages an entirely aqueous acidic solution for carbon fiber recovery. As a demonstration, a small 3-layer CFRP part was fabricated using 6P and 1k plain weave carbon fiber weave following the same composite preparation methods as previously mentioned (Fig. 8a). The 6P CFRP laminates were submerged in 1 M HCl for 12 h to ensure complete degradation of the matrix (Fig. 8a). Upon removal from the 1 M HCl bath, the recovered carbon fiber weaves were easily separated (Fig. 8a), soaked in a DI  $\text{H}_2\text{O}$  bath multiple times, and dried in a 60 °C incubation oven. Fig. 8b and c show the SEM micrographs of the pristine and recovered fibers, respectively. In both cases, the surface morphology is smooth and free of noticeable defects at 1000× magnification. The XPS survey



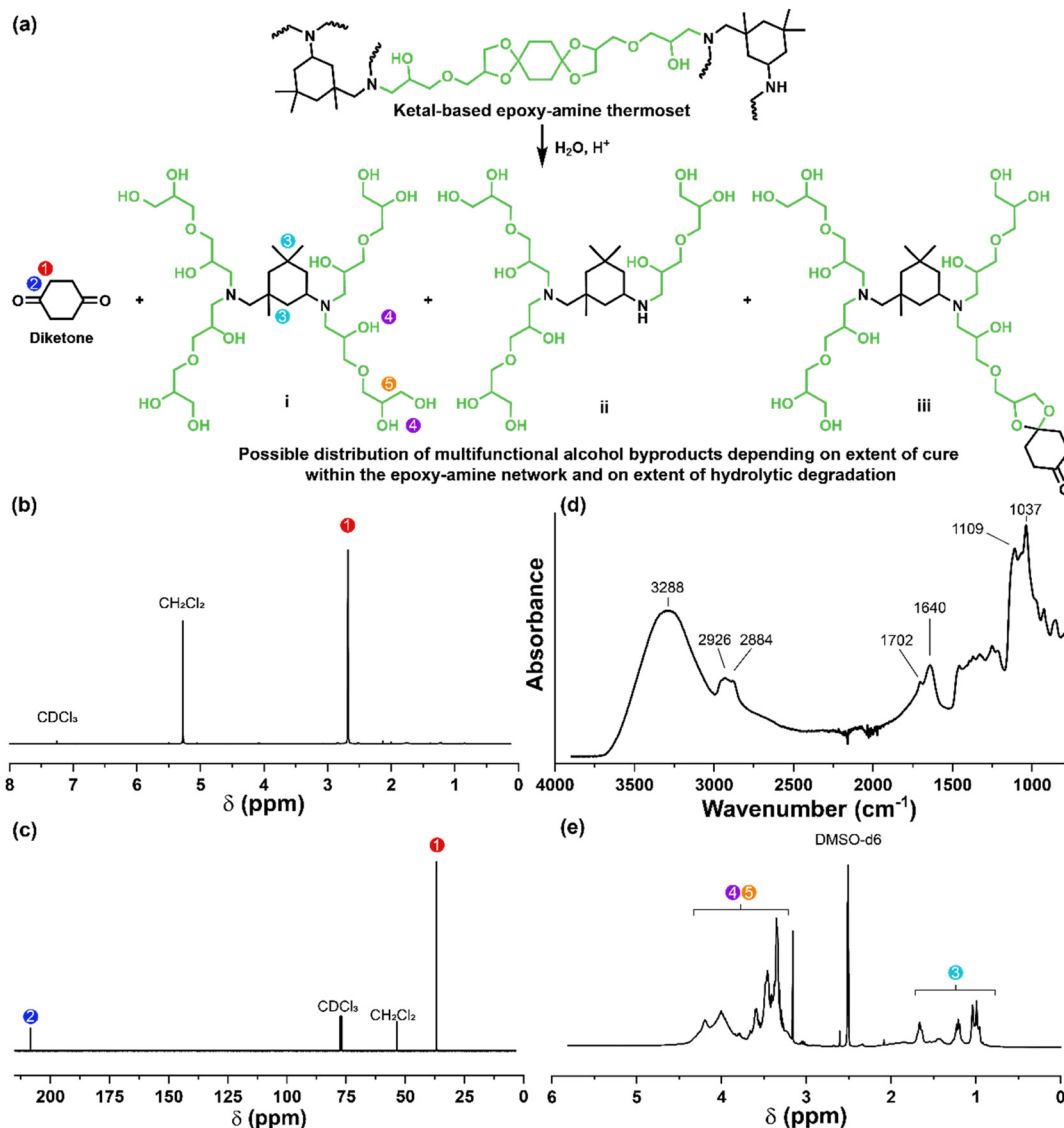


**Fig. 7** (a) Degradation of thermoset **3P** under acidic aqueous conditions to yield 1,4-cyclohexanedione and a mixture of multifunctional alcohol structures. (b)  $^1\text{H}$  NMR of 1,4-cyclohexanedione obtained from the organic phase. (c)  $^{13}\text{C}$  NMR of 1,4-cyclohexanedione obtained from the organic phase. (d) FTIR of the multifunctional alcohol mixture obtained after lyophilization of the neutralized aqueous phase. (e)  $^1\text{H}$  NMR of the multifunctional alcohol mixture; due to the inability to separate the products, only general NMR peak assignments are made.

spectrum of the pristine carbon fibers is shown in Fig. 8d indicating the presence of carbon (C 1s, 80.45 at%), oxygen (O 1s, 18.88 at%), and nitrogen (N 1s, 0.68 at%). XPS analysis of the carbon fiber recovered after degradation of the **6P** matrix, as shown in Fig. 8e, revealed a similar elemental composition with a small increase in the nitrogen content, likely due to residual polymer degradation by-products. Considering the simplicity of the recovery process (*e.g.*, fiber weaves were simply soaked in DI water with minimal agitation as to not disrupt the weave), the recovered fibers were remarkably clean and unperturbed.

In the previous section, we demonstrated the hydrolytic stability of the ketal-based epoxy-amine thermosets, which remained stable for over 800 hours in conditions ranging from

pH 4 to pH 12 but rapidly degraded at pH 1. Additionally, we demonstrated the ability to induce degradation of the polymer matrix and recovery of near-pristine carbon fibers using entirely aqueous conditions. To illustrate the practical application of these ketal-based epoxy-amine thermosets, we fabricated CFRP composites to replace several acrylonitrile butadiene styrene (ABS) plastic components on first author Alameda's motorcycle (Fig. 9). This real-world application served as a rigorous test of durability and performance of these ketal-based CFRPs under demanding conditions (weather, temperature, *etc.*). Albeit a qualitative assessment, the ketal-based CFRP components have shown no signs of degradation, either in appearance or performance after two years of use. This successful application underscores the





**Fig. 8** (a) Degradation of a 6P CFRP laminate part *via* submersion in 1 M HCl showing full dissolution of the polymer matrix and separation of carbon fiber layers after washing with DI water and drying. SEM of (b) pristine carbon fibers and (c) carbon fibers recovered after polymer thermoset hydrolysis. XPS survey analysis of (d) pristine and (e) recovered carbon fibers.

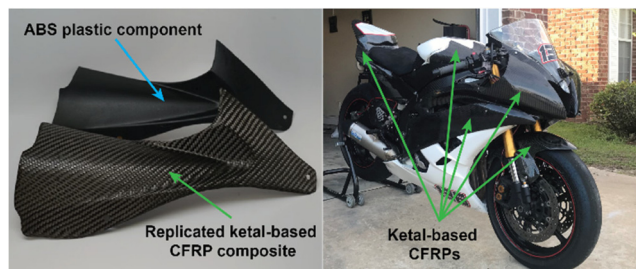


**Fig. 9** (left) Photo of a ketal-based CFRP composite replicated from an original ABS motorcycle component and install. Multiple ketal-based CFRP components were installed on the motorcycle shown (right) and have been field tested approximately two years (at time of manuscript submission).

potential of these ketal-based epoxy-amine thermosets for use in high-performance applications, clearly illustrating opportunities to balance durability and end-of-life recyclability.

## Conclusions

This work demonstrates the successful synthesis and application of degradable epoxy-amine thermosets using novel cyclic-ketal based bisepoxide monomers. These thermosets, exhibiting robust mechanical and thermomechanical properties, provide a promising alternative to non-degradable commercial epoxy-amine thermoset for a broad range of applications. Importantly, the ability to completely degrade these

thermosets in low pH conditions enables the recovery of pristine carbon fibers from CFRPs and the potential to recover and reuse ketone building blocks. The findings underscore the potential utility of cyclic-ketal based thermosets in the fabrication of recyclable CFRP composites clearly illustrating the possibility of achieving balance between real-world application and effective end-of-use carbon fiber recovery strategies.

## Experimental

### Materials

All reagents were obtained commercially and used without further purification unless otherwise specified. 1,4-Cyclohexanedione, 4,4'-bicyclohexanone, 1,4-diacetylbenzene, and isophoronediamine were sourced from TCI Chemical. Tetrabutylammonium bromide (TBAB), epichlorohydrin (EPH), benzene, glycerol, *p*-toluenesulfonic acid (*p*-TsOH) were sourced from Sigma-Aldrich. Potassium hydroxide, 1 M HCl, PBS buffer, glycine, acetic acid, sodium acetate, and other solvents were sourced from Fisher Scientific. 3k 2 × 2 twill weave and 1k plain weave carbon-fiber cloths were supplied from Toray. Hydrogenated diglycidyl ether bisphenol-A (HDGB/Eponex™ 1510) was supplied from Hexion. Deuterated solvents were sourced from Acros.

### Monomer characterization

Monomer structure and purity were confirmed using <sup>1</sup>H-NMR, <sup>13</sup>C-NMR experiments using a Bruker Avance™ 600 and 400 MHz spectrometers. NMR samples were prepared in either deuterated chloroform or deuterated dimethyl sulfoxide. Additionally, monomer structure was confirmed by mass spectrometry using a Bruker 12 Tesla APEX-Qe FTICR-MS in positive-ion mode ionization with an Apollo II ion source.

### Synthesis of monomer 3

30.0 g (0.27 mol) of 1,4-cyclohexanedione (**1**) was added to a 250 mL RBF with 65.0 g (0.71 mol) glycerol, a catalytic amount of *p*-TsOH, and 150 mL benzene. The reaction was purged under a constant flow of N<sub>2</sub> and refluxed using a Dean-Stark trap to collect water. The extent of the reaction measured *via* the total water produced from the reaction. Once the reaction was complete, it was allowed to cool to room temperature with 4 mL of triethylamine added to quench the *p*-TsOH. The benzene was then removed from the reaction using a rotary evaporator with 100 mL ethyl acetate added back to the reaction to redissolve the product. The reaction was then washed 3× with DI water and 3× with brine. The aqueous layer was extracted 3× with ethyl acetate and combined with the remaining organic layer and dried using sodium sulfate. The excess solvent was removed under vacuum to yield 51.3 g (0.20 mol) of a yellowish, viscous oil (intermediate product **2**, yield: 73.9%). NMR characterization of the purified intermediate **2** is provided in the ESI† and is in agreement with data previously reported by Lingier *et al.*<sup>50</sup> and Hu *et al.*<sup>51</sup> Without further purification, 30 g (0.12 mol) of **2** was then added to a 500 mL



RBF with 55.6 g (0.60 mol) EPH and 3.00 g (0.009 mol) TBAB and stirred at 100 °C for 5 h after which the solution turned a pale yellowish color. The reaction was cooled to 0 °C in an ice bath under mechanical overhead stirring. Once cooled a 50 : 50 KOH : H<sub>2</sub>O solution was added dropwise while stirring and allowed to stir for 72 h. The reaction was filtered to remove the KCl precipitate and then washed 3× with DI H<sub>2</sub>O and 3× with brine, dried with sodium sulfate, and placed under reduced pressure at 40 °C to remove solvent and excess EPH to yield crude monomer **3**. Purification by column chromatography (15 : 85 hexane : ethyl acetate) was used to purify the final product to yield 29.5 g (0.8 mol) of a clear oil (yield: 66.0%). HRMS: calcd for C<sub>18</sub>H<sub>28</sub>O<sub>8</sub>Na<sup>+</sup> [M + Na]<sup>+</sup> *m/z*: 395.167639, measured: 395.167319. <sup>1</sup>H NMR (600 MHz, CDCl<sub>3</sub>) δ 4.31–4.24 (m, 2H), 4.05 (ddt, *J* = 8.2, 6.4, 1.6 Hz, 2H), 3.84 (t, *J* = 2.7 Hz, 0.5H), 3.84–3.81 (m, 1H), 3.80 (dd, *J* = 2.9, 1.1 Hz, 0.5H), 3.75 (ddd, *J* = 9.6, 8.3, 6.3 Hz, 2H), 3.63 (dd, *J* = 10.1, 5.5 Hz, 1H), 3.57 (dd, *J* = 5.5, 2.0 Hz, 2H), 3.54–3.49 (m, 1H), 3.48–3.39 (m, 2H), 3.15 (dtq, *J* = 5.8, 2.9, 1.4 Hz, 2H), 2.80 (ddd, *J* = 5.2, 4.2, 1.4 Hz, 2H), 2.61 (dq, *J* = 4.9, 2.5 Hz, 2H), 1.91–1.70 (m, 8H). <sup>13</sup>C NMR (151 MHz, CDCl<sub>3</sub>) δ 108.93 (C), 74.39 (CH), 72.25 (CH<sub>2</sub>), 72.14 (CH<sub>2</sub>), 66.33 (CH<sub>2</sub>), 50.64 (CH), 43.91 (CH<sub>2</sub>), 33.33 (CH<sub>2</sub>), 31.84 (CH<sub>2</sub>).

#### Synthesis of monomer 6

15.3 g (0.079 mol) of 4,4'-bicyclohexanone (**4**) was added to a 250 mL RBF with 23 g (0.25 mol) glycerol, a catalytic amount of *p*-TsOH, and 80 mL benzene. The reaction was purged under a constant flow of N<sub>2</sub> and refluxed using a Dean–Stark trap to collect water. The extent of the reaction measured *via* the total water produced from the reaction. Once the reaction was complete, it was allowed to cool to room temperature with 5 mL of triethylamine added to quench the *p*-TsOH. The benzene was then removed from the reaction using a rotary evaporator with 100 mL ethyl acetate added to redissolve the product. The reaction was then washed 3× with DI H<sub>2</sub>O, 3× with brine and dried using sodium sulfate. The excess solvent was removed under vacuum to yield 22.07 g (0.064 mol) of pure intermediate product **5**, a white powder (yield 81.0%). 10.0 g (0.029 mol) of intermediate product **5** was then added to a 250 mL RBF with 42.1 g (0.45 mol) EPH and 1.00 g (0.003 mol) TBAB was stirred at 100 °C for 5 h. The reaction was then cooled to 0 °C in an ice bath under mechanical stirring. Once cooled a 50 : 50 KOH : H<sub>2</sub>O solution was added dropwise with mechanical overhead stirring and allowed to stir for 48 h. The reaction was filtered to remove the KCl precipitate and then washed 3× with H<sub>2</sub>O and 3× with brine, dried with sodium sulfate, and placed under reduced pressure at 40 °C to remove solvent and excess EPH to yield crude monomer **6**. Purification by column chromatography (15 : 85 hexane : ethyl acetate) was used to purify the final product to yield 9.81 g (0.021 mol) of a clear oil (yield: 74.4%). HRMS: calcd for C<sub>24</sub>H<sub>38</sub>O<sub>8</sub>Na<sup>+</sup> [M + Na]<sup>+</sup> *m/z*: 477.245889, measured: 477.245856. <sup>1</sup>H NMR (600 MHz, CDCl<sub>3</sub>) δ 4.35–4.18 (m, 2H), 4.10–3.99 (m, 2H), 3.88–3.67 (m, 4H), 3.67–3.37 (m, 6H), 3.21–3.09 (m, 2H), 2.80 (q, *J* = 4.2 Hz, 2H), 2.67–2.56 (m, 2H),

1.87–1.76 (m, 2H), 1.76–1.65 (m, 6H), 1.65–1.52 (m, 2H), 1.43 (dtd, *J* = 26.0, 13.1, 4.0 Hz, 2H), 1.37–1.20 (m, 4H), 1.14 (tdd, *J* = 10.6, 6.0, 2.8 Hz, 2H) ppm. <sup>13</sup>C NMR (151 MHz, CDCl<sub>3</sub>) δ 110.08 (C), 74.29 (CH), 72.19 (CH<sub>2</sub>), 66.47 (CH<sub>2</sub>), 50.77 (CH<sub>2</sub>), 44.13 (CH), 41.20 (CH<sub>2</sub>), 35.97 (CH), 34.45 (CH<sub>2</sub>), 27.15 (CH<sub>2</sub>).

#### Synthesis of monomer 9

20.4 g (0.126 mol) of 1,4-diacetylbenzene (**7**) was added to a 500 mL RBF with 25.8 g (0.280 mol) glycerol, a catalytic amount of *p*-TsOH, and 175 mL benzene. The reaction was purged under a constant flow of N<sub>2</sub> and refluxed using a Dean–Stark trap to collect water. The extent of the reaction measured *via* the total water produced. Once the reaction was complete, it was allowed to cool to room temperature and 5 mL of triethylamine added to quench the *p*-TsOH. The reaction was then washed 3× with DI water and 3× with brine and dried using sodium sulfate. The excess solvent was removed under vacuum to yield 30.1 g (0.097 mol) (77.07% yield) of intermediate product **8**, a yellowish viscous oil. All of **8** was then added to a 500 mL RBF with 89.0 g (0.99 mol) EPH, 1.5 g (0.005 mol) TBAB, and cooled to 0 °C in an ice bath under mechanical stirring. Once cooled 40 mL of a 50 : 50 KOH : H<sub>2</sub>O solution was added dropwise while stirring and allowed to react for 48 h. The reaction was filtered to remove the KCl precipitate, 40 mL of dichloromethane (DCM) was added to the reaction and then washed 3× with H<sub>2</sub>O and 3× with brine, dried with sodium sulfate and put under reduced pressure at 40 °C to remove solvent and excess EPH to yield crude monomer **9**. Purification by column chromatography (15 : 85 hexane : ethyl acetate) was used to purify the final product (yield: 19.5 g, 47.6%), a clear viscous oil. HRMS: calcd for C<sub>22</sub>H<sub>30</sub>O<sub>8</sub>Na<sup>+</sup> [M + Na]<sup>+</sup> *m/z*: 445.183289, measured: 445.183002. <sup>1</sup>H NMR (400 MHz, CDCl<sub>3</sub>) δ 7.55–7.36 (m, 4H), 4.50–4.38 (m, 0.5H), 4.25–4.09 (m, 2H), 3.93–3.29 (m, 11.5H), 3.27–3.02 (m, 2H), 2.79 (dt, *J* = 19.4, 4.6 Hz, 1H), 2.70–2.51 (m, 2H), 1.73–1.47 (m, 2H). <sup>13</sup>C NMR (151 MHz, CDCl<sub>3</sub>) δ 143.90 (C), 125.3 (CH), 109.10 (C), 74.90 (CH), 72.25 (CH<sub>2</sub>), 67.76 (CH<sub>2</sub>), 66.10 (CH<sub>2</sub>), 51.10 (CH), 44.66 (CH<sub>2</sub>), 28.00 (CH<sub>3</sub>) ppm.

#### Monomer hydrolysis kinetics

Hydrolysis kinetics for products **2**, **5**, and **8** were measured *via in situ* <sup>1</sup>H-NMR experiments at ambient temperature (20 °C). Each monomer was prepared as a 0.01 M CD<sub>3</sub>CN stock solution where 0.6 mL of solution was added to separate NMR tubes. <sup>1</sup>H-NMR spectra were taken of each to establish a *t*<sub>0</sub> data point after which. 0.2 mL of 0.01 M DCl solution was then added to each NMR tube to initiate hydrolysis. Total hydrolysis for each monomer was tracked by measuring the relative differences in ketal and ketone by-product peak integrations over time.

#### Epoxy-amine thermoset synthesis

Epoxy monomers were mixed 2 : 1 (mol) with IPDA, using a vibratory mixer and then subsequently degassed to remove any air bubbles. The mixture was then added to a PDMS mold and cured at 75 °C for 2 h, 120 °C for 2 h, and then post cured at





Southern Mississippi. MSK acknowledges support from the NSF REU Site: Polymer Innovation for a Sustainable Future (DMR-1950387). Instrumentation was supported by the NSF Major Research Instrumentation program (DMR-1726901) and the US Army Engineer Research and Development Center (ERDC) under ERDC BAA 18-0500 and BAA 20-0110 "Multifunctional Materials to Address Military Engineering" executed under Contract No. W912HZ-18-C-0022 and W912HZ-21-C-0029.

## References

- 1 F. L. Jin, X. Li and S. J. Park, *J. Ind. Eng. Chem.*, 2015, **29**, 1–11.
- 2 Y. Wen, C. Chen, Y. Ye, Z. Xue, H. Liu, X. Zhou, Y. Zhang, D. Li, X. Xie and Y.-W. Mai, *Adv. Mater.*, 2022, **34**, 2201023.
- 3 P. K. Mallick, *Fiber-reinforced composites: materials, manufacturing, and design*, CRC Press, Boca Raton, FL, 3rd edn, 2008.
- 4 R. A. Witik, R. Teuscher, V. Michaud, C. Ludwig and J.-A. E. Månson, *Composites, Part A*, 2013, **49**, 89–99.
- 5 S. Kumar and S. Krishnan, *Chem. Pap.*, 2020, **74**, 3785–3807.
- 6 S. Das, *Int. J. Life Cycle Assess.*, 2011, **16**, 268–282.
- 7 B. Wang, S. Ma, S. Yan and J. Zhu, *Green Chem.*, 2019, **21**, 5781–5796.
- 8 G. Oliveux, L. O. Dandy and G. A. Leeke, *Prog. Mater. Sci.*, 2015, **72**, 61–99.
- 9 P. Yang, Q. Zhou, X.-Y. Li, K.-K. Yang and Y.-Z. Wang, *J. Reinf. Plast. Compos.*, 2014, **33**, 2106–2114.
- 10 Y. Kakichi, A. Yamaguchi, T. Hashimoto, M. Urushisaki, T. Sakaguchi, K. Kawabe, K. Kondo and H. Iyo, *Polym. J.*, 2017, **49**, 851–859.
- 11 A. Yamaguchi, T. Hashimoto, Y. Kakichi, M. Urushisaki, T. Sakaguchi, K. Kawabe, K. Kondo and H. Iyo, *J. Polym. Sci., Part A: Polym. Chem.*, 2015, **53**, 1052–1059.
- 12 S. Pimenta and S. T. Pinho, *Waste Manage.*, 2011, **31**, 378–392.
- 13 S. T. Nguyen, L. R. Fries, J. H. Cox, Y. Ma, B. P. Fors and R. R. Knowles, *J. Am. Chem. Soc.*, 2023, **145**, 11151–11160.
- 14 S. Wang, S. Ma, Q. Li, X. Xu, B. Wang, W. Yuan, S. Zhou, S. You and J. Zhu, *Green Chem.*, 2019, **21**, 1484–1497.
- 15 H. Si, L. Zhou, Y. Wu, L. Song, M. Kang, X. Zhao and M. Chen, *Composites, Part B*, 2020, **199**, 108278.
- 16 M. Kuroyanagi, A. Yamaguchi, T. Hashimoto, M. Urushisaki, T. Sakaguchi and K. Kawabe, *Polym. J.*, 2022, **54**, 313–322.
- 17 P. Li, S. Ma, B. Wang, X. Xu, H. Feng, Z. Yu, T. Yu, Y. Liu and J. Zhu, *Compos. Sci. Technol.*, 2022, **219**, 109243.
- 18 S. Ma, J. Wei, Z. Jia, T. Yu, W. Yuan, Q. Li, S. Wang, S. You, R. Liu and J. Zhu, *J. Mater. Chem. A*, 2019, **7**, 1233–1243.
- 19 M.-S. Wu, B. C. Jin, X. Li and S. Nutt, *Adv. Manuf.: Polym. Compos. Sci.*, 2019, **5**, 114–127.
- 20 K. S. K. Reddy, W.-J. Gao, C.-H. Chen, T.-Y. Juang, M. M. Abu-Omar and C.-H. Lin, *ACS Sustainable Chem. Eng.*, 2021, **9**, 5304–5314.
- 21 H. Nabipour, X. Wang, B. Kandola, L. Song, Y. Kan, J. Chen and Y. Hu, *Polym. Degrad. Stab.*, 2023, **207**, 110206.
- 22 H. Memon, Y. Wei, L. Zhang, Q. Jiang and W. Liu, *Compos. Sci. Technol.*, 2020, **199**, 108314.
- 23 Y. Liu, F. Lu, L. Yang, B. Wang, Y. Huang and Z. Hu, *ACS Sustainable Chem. Eng.*, 2023, **11**, 1527–1539.
- 24 B. M. Alameda, J. S. Murphy, B. L. Barea-López, K. D. Knox, J. D. Sisemore and D. L. Patton, *Macromol. Rapid Commun.*, 2022, **43**, 2200028.
- 25 B. M. Alameda, T. C. Palmer, J. D. Sisemore, N. G. Pierini and D. L. Patton, *Polym. Chem.*, 2019, **10**, 5635–5644.
- 26 M. M. Kreevoy, C. R. Morgan and R. W. Taft Jr., *J. Am. Chem. Soc.*, 1960, **82**, 3064–3066.
- 27 B. Liu and S. Thayumanavan, *J. Am. Chem. Soc.*, 2017, **139**, 2306–2317.
- 28 D. Rana, V. Sauvart and J. L. Halary, *J. Mater. Sci.*, 2002, **37**, 5267–5274.
- 29 J. Karger-Kocsis, O. Gryshchuk and N. Jost, *J. Appl. Polym. Sci.*, 2003, **88**, 2124–2131.
- 30 H. G. Chae, B. A. Newcomb, P. V. Gulgunje, Y. Liu, K. K. Gupta, M. G. Kamath, K. M. Lyons, S. Ghoshal, C. Pramanik, L. Giannuzzi, K. Şahin, I. Chasiotis and S. Kumar, *Carbon*, 2015, **93**, 81–87.
- 31 P. K. Mallick, *Fiber-Reinforced Composites: Materials, Manufacturing, and Design*, CRC Press, Boca Raton, 3rd edn, 2007.
- 32 N. Mattar, V. Langlois, E. Renard, T. Rademacker, F. Hübner, M. Demleitner, V. Altstädt, H. Ruckdäschel and A. Rios de Anda, *ACS Appl. Polym. Mater.*, 2021, **3**, 426–435.
- 33 M. S. Madhukar and L. T. Drzal, *J. Compos. Mater.*, 1991, **25**, 958–991.
- 34 F. von Burkersroda, L. Schedl and A. Göpferich, *Biomaterials*, 2002, **23**, 4221–4231.
- 35 A. Göpferich, in *The Biomaterials: Silver Jubilee Compendium*, ed. D. F. Williams, Elsevier Science, Oxford, 1996, pp. 117–128. DOI: [10.1016/B978-008045154-1.50016-2](https://doi.org/10.1016/B978-008045154-1.50016-2).
- 36 M. P. Torres, B. M. Vogel, B. Narasimhan and S. K. Mallapragada, *J. Biomed. Mater. Res., Part A*, 2006, **76A**, 102–110.
- 37 J. G. Pritchard and I. A. Siddiqui, *J. Chem. Soc., Perkin Trans. 2*, 1973, 452–457, DOI: [10.1039/P29730000452](https://doi.org/10.1039/P29730000452).
- 38 E. Cordes and H. Bull, *Chem. Rev.*, 1974, **74**, 581–603.
- 39 M. M. Kreevoy, *J. Am. Chem. Soc.*, 1956, **78**, 4236–4239.
- 40 M. M. Kreevoy and R. W. Taft Jr., *J. Am. Chem. Soc.*, 1955, **77**, 5590–5595.
- 41 M. S. Newman and R. J. Harper Jr., *J. Am. Chem. Soc.*, 1958, **80**, 6350–6355.
- 42 T. H. Fife and L. Hagopian, *J. Org. Chem.*, 1966, **31**, 1772–1775.
- 43 T. H. Fife and L. Jao, *J. Org. Chem.*, 1965, **30**, 1492–1495.
- 44 D. N. Amato, D. V. Amato, Y. Adewunmi, O. V. Mavrodi, K. H. Parsons, S. N. Swilley, D. A. Braasch, W. D. Walker, D. V. Mavrodi and D. L. Patton, *ACS Appl. Bio Mater.*, 2018, **1**, 1983–1991.



- 45 G. Socrates and G. Socrates, *Infrared and Raman characteristic group frequencies: tables and charts*, Wiley, Chichester, New York, 3rd edn, 2001.
- 46 W. Lu, P. Zhu, Y. Zhao, D. Wang and X. Dong, *Chem. – Eur. J.*, 2023, **29**, e202300622.
- 47 X. Kuang, E. Guo, K. Chen and H. J. Qi, *ACS Sustainable Chem. Eng.*, 2019, **7**, 6880–6888.
- 48 Q. Zhou, X. Zhu, W. Zhang, N. Song and L. Ni, *ACS Appl. Polym. Mater.*, 2020, **2**, 1865–1873.
- 49 T. Hashimoto, H. Meiji, M. Urushisaki, T. Sakaguchi, K. Kawabe, C. Tsuchida and K. Kondo, *J. Polym. Sci., Part A: Polym. Chem.*, 2012, **50**, 3674–3681.
- 50 S. Lingier, Y. Spiesschaert, B. Dhanis, S. De Wildeman and F. E. Du Prez, *Macromolecules*, 2017, **50**, 5346–5352.
- 51 X. Hu, T. Yang, R. Gu, Y. Cui, C. Yuan, H. Ge, W. Wu, W. Li and Y. Chen, *J. Mater. Chem. C*, 2014, **2**, 1836–1843.
- 52 D. Bücheler, A. Kaiser and F. Henning, *Composites, Part B*, 2016, **106**, 218–223.

